The Effects of Ocean Surface Waves on Global Intraseasonal Prediction: Case Studies with a Coupled CFSv2.0-WW3 System

Ruizi Shi[1], Fanghua Xu[1*], Li Liu[1], Zheng Fan[1], Hao Yu[1], Hong Li[1,3], Xiang Li[2] and Yunfei Zhang[2]

[1] Ministry of Education Key Laboratory for Earth System Modeling, and Department of Earth System Science, Tsinghua University, Beijing, 100084, China

[2] Key Laboratory of Marine Hazards Forecasting, National Marine Environmental Forecasting Center, Ministry of Natural Resources, Beijing, 100081, China

[3] Department of Atmospheric and Oceanic Sciences and Institute of Atmospheric Sciences, Fudan University, Shanghai, 200433, China.

**Correspondence to*: Fanghua Xu (fxu@mail.tsinghua.edu.cn)

Abstract. This article describes the implementation of a coupling between a global forecast model (CFSv2.0) and a wave model (WW3), and investigates the effects of ocean surface waves on the air-sea interface in the new framework. Several major wave-related processes, including the Langmuir mixing, the Stokes-Coriolis force with entrainment, air-sea fluxes modified by the Stokes drift and momentum roughness length, are evaluated in two groups of 56-day experiments, one for boreal winter and the other for boreal summer. Comparisons are made against in-situ buoys, satellite measurements and reanalysis data, to evaluate the influence of waves on intraseasonal prediction of sea surface temperature (SST), 2-m air temperature (T02), mixed layer depth (MLD), 10-m wind speed (WSP10) and significant wave height (SWH). The wave-coupled experiments show that overestimated SSTs and T02s, as well as underestimated MLDs at mid-high latitudes in summer from original CFSv2.0 are significantly improved due to enhanced vertical mixing generated by the Stokes drift. For WSP10s and SWHs, the wave-related processes generally reduce biases in regions where WSP10s and SWHs are overestimated. On one hand, the decreased SSTs stabilize the marine atmospheric boundary layer, weaken WSP10s and then SWHs. On the other hand, the increased roughness length due to waves reduces the originally overestimated WSP10s and SWHs. In addition, the effects of the Stokes drift and current on air-sea fluxes also rectify WSP10s and SWHs. These cases are helpful for the future development of the two-way CFSv2.0-wave coupled system.

1 Introduction

Ocean surface gravity waves play an important role in modifying physical processes at the atmosphere-ocean interface, which can influence momentum, heat and freshwater fluxes across the air-sea interface (Li and Garrett, 1997; Taylor and Yelland, 2001; Moon et al., 2004; Janssen 2004; Belcher et al., 2012; Moum and Smyth, 2019). For instance, ocean surface waves modify ocean surface roughness to influence the marine atmospheric boundary layer and thus change the momentum, latent heat, and sensible heat transfer (Janssen 1989, 1991; Taylor and Yelland, 2001; Moon et al., 2004; Drennan et al., 2003, 2005). The breaking waves inject turbulent kinetic energy in the upper ocean, which enhances the mixing process (Terray et al. 1996). Nonbreaking surface waves also affect mixing in the upper ocean by adding a wave-related Reynolds stress (Qiao et al., 2004; Ghantous and Babanin, 2014). The wave-related Stokes drift interacts with Coriolis force and produces the Stokes-Coriolis force (Hasselmann 1970). The shear of the Stokes drift is critical for generation of Langmuir circulation, which significantly deepens the mixed layer by strong vertical mixing both at climate scales (Li and Garrett 1997; Belcher et al., 2012) and at weather scales (Kukulka et al., 2009).

Various wave-related parameterizations have been proposed and used in modelling. The wave-related Charnock parameter (C_{ch}) defines sea surface roughness and affects wind stress estimates (Pineau-Guillou et al. 2018; Sauvage et al. 2020). There are primarily three methods for defining C_{ch}, considering the wave-induced kinematic stress (Janssen 1989, 1991), the wave age (Drennan et al., 2003, 2005; Moon et al., 2004), or the steepness (Taylor and Yelland, 2001). The former two are based on the wind-sea conditions, whereas the latter includes both swells and wind-sea waves. Modifications to these Charnock parameterizations were suggested in recent studies for the leveling off roughness under high winds (e.g., Fan et al., 2012; Bidlot et al., 2020; ECMWF, 2020; Li et al., 2021). In the oceanic boundary layer, waves

influence upper ocean mixing via wave dissipation and the Stokes drift-induced processes. In Breivik et al. (2015), the wave dissipation-related turbulent kinetic energy flux is found to yield the largest sea surface temperature (SST) differences in the extratropics. The Stokes drift-induced Langmuir turbulence can improve temperature simulation over most of the world oceans, particularly in the Southern Ocean (Belcher et al., 2012; Li et al., 2016). Polonichko (1997), Van Roekel et al. (2012) and Li et al. (2017) indicated that the Langmuir cell intensity strongly depends on the alignment of winds and waves, reaching a maximum when they are aligned. Li et al. (2016) found the effect of Langmuir cell can be further enhanced by entrainment. In Couvelard et al. (2020), the Stokes drift-related forces can also contribute modestly to the deepening of the mixed layer depth (MLD). In the First Institute of Oceanography Earth System Model, Bao et al. (2019) indicated that the non-breaking wave-induced mixing, the Stokes drift-affected air-sea fluxes, as well as sea spray are all important for climate estimates.

The wave-related processes at the air-sea interface are complex and important in global coupled systems (e.g., Breivik et al. 2015; Law-Chune and Aouf, 2018; Bao et al. 2019; Couvelard et al. 2020). Most of the coupled models with a wave component at global scale were developed for climate research (e.g., Law-Chune and Aouf, 2018; Bao et al. 2019; Couvelard et al. 2020). Exceptionally, an Integrated Forecasting System (IFS) with fully coupled atmosphere, ocean and wave components, developed by European Centre for Medium-Range Weather Forecasts (ECMWF) (Janssen 2004; Bidlot et al. 2019, 2020), has been assembled for global forecasts from medium-range weather scales to seasonal scales (Breivik et al. 2015). The National Centers for Environmental Prediction (NCEP) is establishing its atmosphere-ocean-wave system, in which the Global Forecast System (GFS; the atmosphere module in the Climate Forecast System model version 2.0) is one-way coupled with the WAVEWATCH III (WW3).

The effects of wave-related processes are worth further evaluation in different global coupled

modelling systems. Since it takes significant time for the wave energy to develop (Janssen 2004), we investigate the impact of individual wave processes at intraseasonal timescale in a new global atmosphere-ocean-wave system. To achieve this, we couple WW3 to the Climate Forecast System model version 2.0 (CFSv2.0) and then conduct sensitivity experiments in boreal winter and summer for comparison. The effects of upper ocean mixing modified by Langmuir cell, the Stokes-Coriolis force and entrainment, air-sea fluxes modified by surface current and the Stokes drift, and momentum roughness length are evaluated. The CFSv2.0 is a coupled system mainly applied for intraseasonal and seasonal prediction (e.g., Saha et al. 2014). Our work can provide insights for two-way wave coupling of CFSv2.0, and is helpful for the future development of the CFSv2.0-wave coupling system. Two groups of 56-day predictions are conducted for boreal winter and boreal summer, respectively. Then, the predictions are compared with observations and reanalysis data. For each group, sensitivity experiments with different wave parameterizations are carried out to evaluate the effects of individual wave-related process.

The rest of the paper is structured as follows: methods and numerical experiments with different parameterizations are described in Section 2; the observations and reanalysis data are introduced in Section 3, and the results of experiments are evaluated and compared in Section 4. Finally, a summary and discussion are given in Section 5.

2 Methods and Experiments

2.1 Coupling WAVEWATCH III with CFSv2.0

The version 5.16 of WW3 (WAVEWATCH III Development Group, 2016) developed by the National Oceanic and Atmospheric Administration (NOAA)/NCEP has been incorporated into the CFSv2.0 (Saha et al., 2014) as a new model component. The latitude range of WW3 is 78°S-78°N with a spatial

resolution of 1/3°; the frequency range is 0.04118-0.4056Hz and the total number of frequencies is 25; the number of wave directions is 24 with a resolution of 15°; the maximum global time step and the minimum source term time step are both 180 s.

The CFSv2.0 contains two components, the GFS (details are available at http://www.emc.ncep.noaa.gov/GFS/doc.php) as the atmosphere component and the Modular Ocean Model version 4 (MOM4; Griffies et al., 2004) as the ocean component. MOM4 is integrated on a nominal 0.5° horizontal grid with horizontal resolution enhanced to 0.25° in the tropics, and has 40 vertical levels; the vertical spacing is 10 m in the upper 225 m, and then increases in unequal intervals to the bottom at 4478.5 m. A three-layer sea ice model is included in MOM4 (Wu et al. 2005). GFS uses a spectral triangular truncation of 382 waves (T382) in the horizontal, which is equivalent to a grid resolution of nearly 35 km, and 64 sigma-pressure hybrid layers in the vertical. The time steps of both MOM4 and GFS are 180 s. The ocean and atmosphere components are then coupled at the same rate. In the original two-way coupled system, GFS receives SST from MOM4 and sends fluxes of heat, momentum, freshwater to MOM4 (black arrows in Fig. 1).

The Chinese Community Coupler version 2.0 (C-Coupler2; Liu et al., 2018) is used to interpolate and pass variables between atmosphere and wave components as well as ocean and wave components. Each component receives inputs and supplies outputs on its own grids. The C-Coupler2 is a common, flexible and user-friendly coupler, which contains a dynamic 3-D coupling system and enables variables to remain conserved after interpolation.

A schematic diagram of the coupled atmosphere-ocean-wave system is shown in Fig. 1. As illustrated, WW3 is two-way coupled with MOM4 and GFS, through the C-Coupler2. WW3 is forced by 10-m wind from GFS (green arrows) and surface current from MOM4 (blue arrows), and generates the wave action

density spectrum. Meanwhile, the surface Stokes drift velocity, the Stokes transport and the turbulent Langmuir number are passed to MOM4 (red arrows; see Section 2.3) from WW3, and the surface Stokes drift velocity and the Charnock parameter are passed to GFS (red arrows; see Section 2.4 and 2.5). The high frequency tail assumption for the Stokes drift in WW3 is used with a spectral level decaying as f^{-5} (frequency). Additionally, the regular ocean surface current velocities from MOM4 are also passed to GFS, to calculate the relative wind velocity for the turbulent fluxes together with the surface Stokes drift (blue arrows; see Section 2.4).

Both the CFSv2.0 and WW3 use warm starts; the initial fields at 00:00 UTC of the first day in each experiment for CFSv2.0 were generated by the real time operational Climate Data Assimilation System (Kalnay et al., 1996), downloaded from the CFSv2.0 official website (http://nomads.ncep.noaa.gov/pub/data/nccf/com/cfs/prod). To get initial conditions for WW3, a stand-alone WW3 model is set up synchronously (see Section 2.2). Since the interactions between waves and sea ice are complicated and beyond the scope of the study, we turn off the coupling between WW3 and CFSv2.0 in areas with sea ice.

In addition, to properly select the coupling frequency between CFSv2.0 and WW3, the root mean square errors (RMSEs) of SST, significant wave height (SWH) and 10-m wind speed (WSP10) with different coupling steps for the fully coupled experiment (ALL; details in Section 2.6) are calculated and compared (Table S1 of the supplementary material). The three components are coupled every time step (180 s) in 1_STEP_ALL experiment, every 5 steps (900 s) in 5_STEP_ALL experiment and every 10 steps (1800 s) in 10_STEP_ALL experiment. In 10_STEP_WW3, only the WW3 is coupled every 10 time steps, whereas the GFS and the MOM4 remain the one time step (180 s) coupling frequency as the original settings in CFSv2.0. From Table S1, the 10_STEP_WW3 experiment has a relatively short

143 runtime and small RMSEs. Therefore, the time steps of the 10_STEP_WW3 are selected to compromise
144 computing time consumption and model RMSEs.

145 **2.2 Initialization of WAVEWATCH III**

146 In WW3, input of momentum and energy by wind, and dissipation for wave-ocean interaction are two
147 important terms (combined as input-dissipation source term) in the energy balance equation
148 (WAVEWATCH III Development Group, 2016), which includes the estimation of the Charnock
149 parameter. Several different packages to calculate the input-dissipation source term (ST) are available in
150 the WW3 version 5.16, including ST2 (Tolman and Chalikov, 1996), ST3 (Janssen, 2004; Bidlot, 2012),
151 ST4 (Ardhuin et al., 2010), and ST6 (Zieger et al., 2015).

152 The initial wave fields are generated from 10-day simulation starting from rest in a stand-alone WW3
153 model. To minimize the biases of initial wave fields, we test simulations with ST2, ST3, ST4, and ST6
154 schemes respectively, and compare the results with Janson-3 observations. Two 10-m wind datasets, the
155 Cross-Calibrated Multi-Platform (CCMP; Atlas et al., 2011) data and the fifth generation European
156 Centre for Medium-Range Weather Forecasts (ECMWF) Reanalysis (ERA5; Hersbach et al., 2020) data,
157 are used to drive the wave model respectively. Comparing all results, the ST4 scheme with ERA5 wind
158 forcing generates the minimum SWH bias (Table S2 in the supplementary material), consistent with
159 findings in Stopa et al. (2016). Thus, the ST4 scheme is chosen to calculate the input and dissipation
160 term, and generate initial wave fields with ERA5 wind forcing for experiments listed in Table 1. The
161 parameters used for ST4 scheme follow TEST471f from WAVEWATCH III Development Group (2016),
162 which is the CFSR (CFS Reanalysis) tuned setup and is commonly-used at global scale.

2.3 Parameterizations of the Stokes Drift-Related Ocean Mixing

The full Stokes drift profile used in MOM4 is obtained by the method of Couvelard et al. (2020), which is based on the work of Breivik et al. (2014; 2016). Breivik et al. (2016) derived the full Stokes drift profile as

$$u_s B16(z) = u_s(0)[\exp(2k_p z) - \sqrt{-2\pi k_p z}\,\mathrm{erfc}(\sqrt{-2k_p z})], \qquad (1)$$

where $u_s(0)$ is the surface Stokes drift velocity, $k_p = \frac{u_s(0)}{6V_s}$, V_s is the Stokes transport, and erfc is the complementary error function. Eqn. 1 is depth-averaged within each vertical grid interval as

$$u_s(z) = \frac{u_s(0)}{(th)_k}[I(z_{k+1/2}, k_p) - I(z_{k-1/2}, k_p)], \qquad (2)$$

$$I(z, k_p) = \frac{1}{6k_p}[e^{2k_p z} + 4k_p z\frac{u_s B16(z)}{u_s(0)}], \qquad (3)$$

where *th* is the thickness of layer *k*, following Li et al., (2017), Wu et al., (2019) and Couvelard et al., (2020).

2.3.1 Mixing of Langmuir Turbulence

McWilliams and Sullivan (2000) modified the turbulent velocity scale *W* in K-Profile Parameterization (KPP) for vertical mixing by introducing an enhancement factor ε, to account for both boundary layer depth changes and nonlocal mixing by Langmuir turbulence. Based on their work, Van Roekel et al. (2012) improved the enhancement factor corresponding to alignment and misalignment of winds and waves. Li et al. (2016) evaluated these parameterizations in a coupled global climate model, and found that the difference between parameterizations with alignment and with misalignment was not significant, owing to the relatively coarse resolution which cannot accurately represent the refraction by coasts and current features. We use the parameterization from Van Roekel et al. (2012) as well. Because the resolution in our model is relatively coarse too, and the angles between winds and waves are less than

181 30° in most areas (Fig. S1i&j in the supplementary material), we don't consider misalignment in the

182 study.

183 W (W=ku_*/ϕ, where u_* is the surface friction velocity, ϕ is the dimensionless flux profile, and

184 k=0.4 is the von Kármán constant) depends on the turbulent Langmuir number, that is,

$$\mathrm{W} = \frac{ku_*}{\phi}\varepsilon, \tag{4}$$

$$\varepsilon = \sqrt{1 + (3.1La_\mathrm{t})^{-2} + (5.4La_\mathrm{t})^{-4}}, \tag{5}$$

185 where La_t is the turbulent Langmuir number, defined as

$$La_\mathrm{t} = \sqrt{\frac{u_*}{|u_S(0)|}}, \tag{6}$$

186 with $u_s(0)$ the surface Stokes drift velocity.

187 Furthermore, the enhanced W will influence the calculation of boundary layer depth. In KPP the

188 boundary layer depth is determined as the smallest depth at which the bulk Richardson number equals

189 the critical value $Ri_\mathrm{cr} = 0.3$, that is,

$$Ri_b(h) = \frac{gh[\rho_r - \rho(h)]}{\rho_0[|u_r - u(h)|^2 + W^2]} = Ri_\mathrm{cr}, \tag{7}$$

190 where g is acceleration of gravity, ρ is density, u is velocity, ρ_r is surface density, u_r is surface

191 velocity, ρ_0 is the average value of the density and h is the boundary layer depth. Hence, when W is

192 enhanced, the boundary layer depth h is deepened accordingly.

193 **2.3.2 The Stokes-Coriolis Force and Associated Entrainment**

194 Because the Stokes drift velocity is an increment superimposed on the original current velocity, the

195 Coriolis force and the Stoke drift together produce an additional so-called Stokes-Coriolis (SC) force

196 (Hasselmann 1970), that is,

$$SC\ Force = \overrightarrow{\mathrm{u_s(z)}} \times f\vec{z}. \quad (8)$$

197 Here $\overrightarrow{\mathrm{u_s(z)}}$ is the Stokes drift velocity vector, f is the Coriolis frequency, and $\vec{z}$ is the vertical unity
198 vector. For consistency, the Stokes drift velocity is also included in advection terms of tracers (e.g.,
199 temperature, salinity) and convergence terms (Law-Chune and Aouf, 2018; Couvelard et al., 2020). And
200 the free surface condition for barotropic mode is correspondingly modified to

$$\frac{\partial \eta}{\partial t} = -\nabla \mathrm{M_{curr}} - \nabla \mathrm{M_{st}}, \quad (9)$$

201 where η is surface elevation, $\mathrm{M_{curr}}$ and $\mathrm{M_{st}}$ are the total vertical integral of the regular Eulerian
202 current and the Stokes drift, respectively.

203 To depict the entrainment below the ocean surface boundary layer induced by the Stokes drift, Li et
204 al. (2016) suggested adding the square of the surface Stokes drift velocity ($|u_s(0)|^2$) to the denominator
205 of Eqn. 7, that is,

$$Ri_b(h) = \frac{gh[\rho_r - \rho(h)]}{\rho_0[|u_r - u(h)|^2 + W^2 + |u_s(0)|^2]} = Ri_{\mathrm{cr}}. \quad (10)$$

206 The boundary layer depth h in KPP from Eqn. 10 is then enhanced due to the Stokes drift velocity.

207 **2.4 The Stokes Drift and Sea Surface Current on Air-Sea Fluxes**

208 At the air-sea boundary layer, the momentum flux (τ), sensible heat flux (SH) and freshwater flux (E)
209 are calculated as

$$\tau = \rho_a C_d |\Delta\vec{V}| \Delta\vec{V}, \quad (11)$$

$$SH = \rho_a C_h |\Delta\vec{V}| \Delta\theta, \quad (12)$$

$$E = \rho_a C_e |\Delta\vec{V}| \Delta q, \quad (13)$$

210 where C_d, C_h, C_e are surface exchange coefficients for momentum, sensible heat and freshwater. ρ_a

is air density. $\Delta\theta, \Delta q$ are potential temperature and humidity differences between air and sea, and $\Delta\vec{V}$ is velocity of air relative to water flow.

In CFSv2.0, $\Delta\vec{V}$ is set to be wind speed ($\overrightarrow{U_{wind}}$). However, the effect of ocean surface current should not be ignored. Luo et al. (2005) first indicated that including ocean surface current ($\overrightarrow{U_{surf}}$) improves estimates of τ and subsequent ocean response. Renault et al. (2016) further indicated that the improvements of τ by $\overrightarrow{U_{surf}}$ also feed back into atmosphere. At present, $\Delta\vec{V} = \overrightarrow{U_{wind}} - \overrightarrow{U_{surf}}$ is widely used in coupled ocean-atmosphere models (e.g., Hersbach and Bidlot, 2008; Takatama et al., 2017; Renault et al., 2021). Furthermore, Bao et al. (2019) indicated that as a part of the sea surface water movement with speed magnitude comparable to surface current in mid-high latitudes, the surface Stokes drift ($\overrightarrow{u_s(0)}$) should also be included, that is,

$$\Delta\vec{V} = \overrightarrow{U_{wind}} - \overrightarrow{U_{surf}} - \overrightarrow{u_s(0)}. \quad (14)$$

To account for the effects of the surface currents and of the Stokes drift, Eqn. 14 is used in the coupled experiments (Table 1). To complete the coupling, the corresponding modification of the tridiagonal matrix (Lemarié 2015) has been implemented in CFSv2.0. Note that the direction of Stokes drift is generally consistent with 10-m wind (Fig. S1i&j in supplementary material), but the directions of surface current and 10-m wind are usually different due to Coriolis effect (Fig. S1g&h). Consequently, the effects of $\overrightarrow{U_{surf}}$ and $\overrightarrow{u_s(0)}$ on $\Delta\vec{V}$ depend on the angles between them and $\overrightarrow{U_{wind}}$.

2.5 Parameterizations of Momentum Roughness

In CFSv2.0, the fluxes of momentum, heat, and freshwater are passed from atmosphere to ocean, and their estimate is critically important. The fluxes are in part determined by surface roughness length, which can be converted to surface exchange coefficients based on the Monin-Obukhov similarity theory (Monin

231 and Obukhov, 1954).

232 **2.5.1 The Momentum Roughness Length in GFS**

233 In GFS, the momentum roughness length z_0 has two terms. The first term z_{ch} is parameterized by
234 the Charnock relationship (Charnock, 1955) representing wave-resulted sea surface roughness, and the
235 second term z_{vis} is the viscous contribution (Beljaars, 1994) for low winds and smooth surface, that is,

$$z_0 = z_{ch} + z_{vis} = \frac{C_{ch}u_*^2}{g} + \frac{0.11\nu}{u_*}. \quad (15)$$

236 Here $C_{ch} = 0.014$ is the constant Charnock parameter, ν is the air kinematic viscosity. The relation of
237 z_0 in GFS versus 10-m wind speed is shown in Fig.2 (black line).

238 **2.5.2 The Charnock Relationship Related to Wave State**

239 When ocean surface waves are explicitly considered, the Charnock parameter C_{ch} is not a constant
240 (Janssen 1989, 1991; Taylor and Yelland, 2001; Moon et al., 2004; Drennan et al., 2003, 2005). In the
241 study, we adopt a method developed by Moon et al. (2004), which considered the surface roughness
242 leveling off under extremely high wind speed (Powell et al., 2003; Donelan et al., 2004). Based on
243 observations, Moon et al. (2004) proposed Eqn. 16 to estimate the Charnock parameter by the wave age
244 $\frac{c_{pi}}{u_*}$ (c_{pi} is the peak phase speed of the dominant wind-forced waves) with constant values of *a* and *b*
245 changing with 10-m wind speed every 5 m/s in the range of 10 m/s to 50 m/s.

$$C_{ch} = a(\frac{c_{pi}}{u_*})^b, \quad (16)$$

246 To obtain continuous values of *a* and *b*, we derive a new relationship (Eqn. 17) to estimate *a* and *b* from
247 10-m wind speed U_{10} by fitting the values in Table 1 of Moon et al. (2004),

$$a = \frac{1}{0.1477{U_{10}}^2 - 0.7395U_{10} - 10.9995},$$
$$b = 1.5661E^{-5}{U_{10}}^3 - 0.002{U_{10}}^2 + 0.1017U_{10} - 1.6182. \quad (17)$$

Because the observations in Moon et al. (2004) were obtained under tropical cyclones, Eqn. 17 is used for U_{10}>15 m/s, whereas the original Charnock relationship of WW3 ST4 scheme (Janssen 1989, 1991) is used for $U_{10} \leq$15 m/s. The revised parameterization is called ST4-M04. Figure S2 in supplementary material shows the C_{ch} distribution obtained by Eqn. 16-17. In general small wind direction variations at low latitudes lead to large wave age and thus low C_{ch}. The situation is opposite at mid-high latitudes.

The relationships between z_0 and U_{10} in GFS, WW3 ST4 scheme (Janssen 1989, 1991) and ST4-M04 scheme are compared in Fig.2. The z_0 in GFS increases relatively slowly with increasing wind speed (black). The value of z_0 from ST4 scheme (purple) increases rapidly with wind speed at high winds. In comparison, in ST4-M04 scheme (blue) the rapid increase of z_0 at high wind speed is obviously restrained, although the mean z_0 is slightly higher than that in GFS at wind speed >10 m/s due to larger C_{ch} (>0.014 in Fig. S2). Furthermore, since the Charnock number is constant in GFS, the standard deviation (STD) of z_0 at a given wind speed is near zero. Since the z_0 is determined only by wind-sea conditions in ST4 and ST4-M04 scheme, the STD at a given wind speed is mainly owing to variations in wind fetch and development stage of sea state. The reduced STDs in ST4-M04 scheme, compared to ST4, imply less sensitivity of z_0 to fetch and sea state. Note that the ST4-M04 is used in GFS, while the z_0 in WW3 is still calculated by the ST4 source term to avoid affecting the balance of adjusted wind input and dissipation.

2.6 Set of Experiments

A series of numerical experiments is conducted to evaluate the effects of aforementioned wave-related

processes on ocean and atmosphere in two 56-day periods, from January 3 to February 28, 2017 and from August 3 to September 28, 2018 for boreal winter and boreal summer, respectively.

The reference experiment (CTRL) is a one-way coupled experiment, in which CFSv2.0 provides 10-m wind and surface current to WW3, whereas no variable is transferred from WW3 to CFSv2.0. The results of CFSv2.0 in CTRL are consistent with the corresponding CFS Reanalysis data (Saha et al., 2010). For each period, four sensitivity experiments are carried out (Table 1). Based on CTRL, the first is the VR12-AL-SC-EN experiment, in which the Langmuir mixing parameterization is used with the Stokes-Coriolis force and entrainment in MOM4. The second is the Z0-M04 experiment, in which the constant C_{ch} in GFS is replaced by C_{ch} from WW3 ST4-M04 scheme. The effect of fluxes in GFS generated by $\Delta\vec{V}$ (Eqn. 14) is tested in the FLUX experiment. The last experiment is the ALL, which includes all three parameterizations.

3 Data

Due to the availability of in situ and reanalysis data in the simulation periods, only sea surface temperature (SST), ocean subsurface temperature and salinity (T/S), 2-m air temperature (T02), 10-m wind speed (WSP10), and significant wave height (SWH) are used to evaluate the simulation results.

The daily average satellite Optimum Interpolation SST (OISST) data are obtained from NOAA, with $0.25° \times 0.25°$ resolution (Reynolds et al., 2007; https://www.ncdc.noaa.gov/oisst). The global Argo observational profiles of T/S (Li et al., 2019) are from China Argo Real-time Data Center (www.argo.org.cn). The ERA5 datasets of T02, WSP10 and SWH with a spatial resolution of 0.5° are also used (Hersbach et al., 2020; https://cds.climate.copernicus.eu/cdsapp#!/dataset/reanalysis-era5-single-levels), which assimilated huge amounts of historical data and thus provided reliable hourly

288 estimates. Additionally, the WSP10 and SWH observations from the available National Data Buoy
289 Center (NDBC) buoy data (https://www.ndbc.noaa.gov) are used for comparison.

290 **4 Experimental Results**

291 In this section, an evaluation of simulation results is presented. Comparisons are made between model
292 results and observations/reanalysis data. The results in the first three days are excluded in the evaluation,
293 since the wave influences are weak at the beginning. Compared with observations or ERA5, the general
294 increase of the biases in all experiments is likely a drift from the initial conditions since no data are
295 assimilated.

296 **4.1 Sea Surface Temperature (SST) and 2-m Air Temperature (T02)**

297 Figure 3a shows the spatial distribution of 53-day (day 4 to day 56) averaged SST biases in CTRL in
298 boreal winter, defined as SST in CTRL minus OISST. The global mean SST bias is approximately 0.32℃,
299 and the average RMSE is about 1.09℃ from day 4 to day 56 in CTRL (Fig. 3a). The simulated SSTs are
300 generally overestimated, and the large biases (>1.0℃) are mainly distributed in the Southern Ocean. In
301 Fig. 3b, the global-averaged RMSEs of CTRL (black) increase with time in the first month and then
302 gradually level off. Compared with CTRL, the RMSEs are reduced continuously in VR12-AL-SC-EN
303 and ALL (yellow and red), but not in Z0-M04 and FLUX (purple and blue).

304 To understand the critical process responsible for the bias reduction in ALL, the SST differences are
305 compared across all four experiments (Fig.3c-f). Clearly, the difference in experiment VR12-AL-SC-EN
306 is similar to that in ALL (Fig. 3c&3f). The spatial correlation coefficient between the SST differences
307 with CTRL of the two experiments (Fig. 3c&3f) is 0.67, significant at 99% confidence level, and the

RMSEs of SST are not different significantly (red and yellow lines in Fig. 3b), indicating the Stokes drift-related parameterizations in VR12-AL-SC-EN mainly contribute to the SST positive bias reduction. This contrasts with Couvelard et al. (2020), where SST overestimations and MLD underestimations are reduced mainly due to the directly modified turbulence kinetic energy scheme. The global mean SST bias in ALL is 0.02 ℃ with RMSE of 1.03℃, and in most areas the SST differences compared with CTRL are significant ($P \leqslant 0.05$) (dotted areas in Fig. 3f). Large SST improvements mainly appear in the Southern Ocean, with a regional RMSE decrease from 1.27 to 1.04 ℃ south of 45°S (Fig. 3f and red line in Fig. 5a). The reduction of overestimated SSTs in CTRL (red in Fig 3a) is because the Stokes drift-related parameterizations in MOM4 inject turbulent kinetic energy into the ocean, which enhance vertical mixing, and subsequently cool the surface waters (Belcher et al., 2012; Li et al. 2016). The modified roughness and relative velocity in Z0-M04 and FLUX also influence upper ocean mixing (Fig. 3d&e) via changing momentum flux, and lead to generally warmer SSTs (purple and blue lines in Fig. 3b&5a). The effect from Stokes drift-related ocean mixing parameterizations dominates SST changes in ALL.

In boreal summer, the global mean SST bias in CTRL is overestimated approximately 0.29℃, and the averaged RMSE from day 4 to day 56 is about 1.19℃. The overestimated SSTs (>1.0℃) mainly occur in the Northern Hemisphere (Fig. 4a). The global-averaged RMSEs are also generally lower in VR12-AL-SC-EN and ALL than in CTRL (Fig. 4b). The cooling effects in VR12-AL-SC-EN lead to a global mean bias of 0.06℃, and the large SST improvements mainly occur north of 50°N (Fig. 4c and yellow line in Fig. 5b). The changes of SST in Z0-M04 and FLUX (Fig. 4d&e; purple and blue lines in Fig. 4b&5b) are relatively small. The global mean bias in ALL is 0.04℃ with an RMSE of 1.14℃ (Fig. 4f).

As aforementioned, large improvements of overestimated SST mainly occur at mid-high latitudes in local summer. The time series of RMSEs and correlation coefficients of SST between model and

observation in the region (0-360°E, 45°-78°S in boreal winter and 0-360°E, 50°-78°N in boreal summer) are shown in Fig. 5c-f. The RMSEs in CTRL (blue in Fig. 5c&d) increase in the first few weeks and then gradually decrease afterward. Compared with CTRL, RMSEs in VR12-AL-SC-EN (yellow) and ALL (red) are significantly ($P \leqslant 0.01$) reduced by about 0.3℃. The spatial correlation coefficients decrease with time but remain high (>0.90) for all experiments (Fig. 5e&f) with higher values in experiment VR12-AL-SC-EN (yellow).

We also compared T02 from experiments with ERA5 (Fig. 6). Warm biases of T02 appear in both winter and summer in CTRL (Fig. 6a&b). The changes of T02 in sensitivity experiments (Fig. 6c-j) are generally consistent with the changes of SST in the same experiments (Fig.3&4). The correlation coefficients between the SST and the T02 changes for the ALL experiment in boreal winter and summer (Fig. 3f&6f and Fig. 4f&6j) are 0.61 and 0.53 respectively, significant at 99% confidence level. In boreal winter, all wave-coupled experiments except FLUX reduce the T02 mean bias (Fig.6c-f). VR12-AL-SC-EC has the largest T02 bias reduction compared with CTRL, from 0.55℃ to 0.17℃ (Fig.6c). In boreal summer, both VR12-AL-SC-EC and ALL have the largest T02 bias reduction, from 0.29℃ to 0.08℃ (Fig.6g&j). Noticeably, the improvements in RMSEs are not large for all experiments, because the improvements mainly occur in areas with overestimated temperature.

4.2 Mixed Layer Depth (MLD)

To further evaluate the direct effect of the wave-related processes on the upper ocean, we compare the MLD of all experiments with that estimated from Argo profiles in summer. The simulated T/S are interpolated onto the positions of Argo profiles at the nearest time. The MLD is estimated as the depth where the change of potential density reaches the value corresponding to a 0.2℃ decrease of potential

temperature with unchanged salinity from surface (de Boyer Montégut et al., 2004; Wang and Xu, 2018).

The time series of MLDs from numerical experiments and Argo south of 45°S in boreal winter (north of 45°N in boreal summer) are compared in Fig. 7a (7b). The simulated MLDs are generally within the STD of Argo MLDs (shading in Fig. 7). In CTRL, the mean bias (CTRL minus Argo) with STD is -13.15±7.82 m (-6.75±5.29 m) in boreal winter (summer). The correlation coefficient of MLDs in CTRL with Argo MLDs is 0.55 (0.68) with $P \leqslant 0.01$, and the mean RMSE is 15.30 m (8.55 m) in boreal winter (summer). In ALL, the mean bias (ALL minus Argo) with STD is 7.70±10.42 m (3.30±7.78 m) in boreal winter (summer), and the correlation coefficient of MLDs enhances to 0.63 (0.78). The RMSE south of 45°S decreases from 15.30 m in CTRL to 12.96 m in ALL. The RMSE north of 45°N decreases from 6.71 m in CTRL to 5.55 m in ALL in the first six weeks but the value increases in the last two weeks due to overestimation of MLDs. Compared with CTRL (orange in Fig. 7), VR12-AL-SC-EN (yellow) and ALL (dark blue) show significant improvements ($P \leqslant 0.01$) on the underestimated MLDs time series, whereas the MLDs difference between CTRL and Z0-M04 (purple)/FLUX (blue) is non-significant.

4.3 Wind Speed at 10 m (WSP10) and Significant Wave Height (SWH)

Compared with ERA5, the WSP10s in CTRL are generally overestimated in both winter and summer (Fig.8a&9a). The global averaged RMSEs of WSP10s in CTRL are 4.25 m/s (4.26 m/s) in boreal winter (summer). The global averaged RMSEs of WSP10s in all experiments increase with time in the first two weeks and then gradually level off (Fig. 8b&9b). The differences of RMSEs between CTRL and other experiments are tiny in the first 10 days, and afterwards the RMSEs in Z0-M04 and ALL (purple and red) become clearly smaller than in CTRL over most of the time.

The comparisons of the simulated SWHs in CTRL with the ERA5 also show that the SWHs are

372 overestimated in both winter and summer (Fig. 10a&11a). In boreal winter, the global mean SWH bias
373 in CTRL is approximately 0.20 m with overestimates (> 0.30 m) in the Pacific, the North Atlantic and
374 the Southern Ocean (Fig.10a), and the average RMSE is about 1.29 m. In boreal summer, the global
375 mean bias in CTRL is approximately 0.17 m with 1.22 m RMSE (Fig. 11a). Similar to WSP10s, the
376 RMSEs of SWHs also increase in the first two weeks and then gradually level off (Fig. 10b&11b). The
377 RMSEs in Z0-M04 and ALL (purple and red) are smaller than in CTRL over most of the time, consistent
378 with changes of WSP10s. The correlation coefficients between changes of WSP10s and changes of
379 SWHs in ALL are 0.77 and 0.73 in boreal winter and summer respectively (Fig. 8f&10f and Fig. 9f&11f),
380 significant at 99% confidence level, indicating that the SWHs changes are closely related to changes of
381 wind speeds.
382 In VR12-AL-SC-EN, the reduction of SST warm biases affects air temperature and stabilizes the
383 marine atmospheric boundary layer (Sweet et al. 1981; O'Neill et al. 2003), and subsequently reduces
384 WSP10s and SWHs with decreased global bias in boreal winter (Fig.8c&10c). In Z0-M04, the
385 overestimated WSP10s and SWHs are also reduced (Fig. 8d&10d) due to the larger z_0 with the ST4-
386 M04 scheme at wind speed > 10 m/s (Fig. 2). The increase of z_0 enhances wind stress and momentum
387 transferred into the ocean, and therefore reduces surface winds (Pineau-Guillou et al. 2018; Sauvage et
388 al. 2020) and consequently reduces SWHs. In FLUX (Fig. 8e&10e), $\overrightarrow{U_{surf}}$ and $\overrightarrow{u_s(0)}$ decrease wind
389 stress and momentum transfer when their directions are consistent with wind directions, and vice versa
390 (Hersbach and Bidlot, 2008; Renault et al., 2016). For instance, the angles between wind and current are
391 relatively small (<90°) in the northeastern Pacific, reducing the wind stress and thus enhancing WSP10s
392 (Fig. 8e). In contrast, the large angles (>90°) between the northwesterlies and the Kuroshio in the
393 northwestern Pacific enhance wind stress, and decrease WSP10s (Fig. 8e). Consequently, improvements

394 occur in areas with misalignment of winds and currents. With all combined effects, the biases of WSP10s
395 and SWHs in ALL in most regions are decreased (Fig. 8f&10f), with the reduced global RMSEs of 4.17
396 m/s and 1.18 m respectively. In boreal summer, the improvements of WSP10s and SWHs are relatively
397 small in terms of global averaged RMSEs, because of smaller positive biases in CTRL (Fig. 9a&11a). In
398 ALL, the global averaged bias of WSP10s (SWHs) is -0.01 m/s (0.03 m). The largest reduction primarily
399 appears in the Southern Ocean (Fig. 9f&11f) to improve the overestimated westerlies and SWHs in CTRL
400 (Fig. 9a&11a).

401 Previous studies indicated that ocean surface winds in ERA5 are underestimated in some regions
402 (Belmonte Rivas and Stoffelen 2019; Kalverla et al. 2020; Sharmar and Markina 2020). To better
403 demonstrate the effects of waves on WSP10s and SWHs, comparisons of WSP10s and SWHs with the
404 NDBC buoy data are made (Table 2 and Fig. 12). The differences between sensitivity experiments and
405 CTRL are all statistically significant at 95% confidence level. Buoys are mainly located in the
406 northeastern Pacific, the tropical Pacific and the northwestern Atlantic oceans (Fig. S3), and buoy
407 identifiers with total numbers, longitudes and latitudes are listed in Table S3. The method from Hsu et al.
408 (1994) is used to adjust wind speeds from buoy data to the reference height of 10 m.

409 Compared to the NDBC data, the WSP10s and the SWHs in CTRL are generally overestimated in both
410 winter and summer with positive mean biases (Table 2 and Fig. 12). The reduction of mean biases appears
411 in all experiments except FLUX in boreal winter. The wave-related processes are most effective in areas
412 with positive biases, consistent with previous comparisons with ERA5. In boreal winter, the angles
413 between winds and currents are small. The wind stresses are then reduced in FLUX, and the WSP10s are
414 enhanced. So the positive bias is further enhanced. The improvements in ALL are generally the largest
415 (Table 2), with the WSP10s RMSE of 1.04 m/s (1.15 m/s) and the SWHs RMSE of 0.36 m (0.24 m) in

boreal winter (summer). As shown in Fig. 12, with the increase of WSP10s and SWHs, the reduction of overestimation in ALL compared with CTRL is more prominent.

5 Summary and Discussion

To investigate the individual role played by wave-related processes on atmosphere and ocean interface in a coupled global atmosphere-ocean-wave modelling system on intraseasonal scale, we implement the version 5.16 of WW3 into CFSv2.0 over the domain 78°S-78°N, using the C-Coupler2. In this coupled system, the WW3 is forced by 10-m wind and surface current generated in CFSv2.0. The Stokes drift-related Langmuir mixing, the Stokes-Coriolis force and entrainment in ocean, air-sea fluxes modified by surface current and the Stokes drift, and momentum roughness length (z_0) are considered separately, and the results of sensitivity experiments are compared against in-situ buoys, satellite measurements and ERA5 reanalysis. The effects of waves on intraseasonal prediction are examined in two 56-day cases, one for boreal winter and the other one for boreal summer.

The following key results are found:

1. Overestimated SST, T02 and underestimated MLD in the mid-high latitudes in CFSv2.0 are significantly improved, particularly in local summer. Because enhanced vertical mixing generated by Langmuir turbulence, Stokes-Coriolis force and entrainment in VR12-AL-SC-EN changes temperature structure in the upper ocean, and further affects air temperature. In boreal winter, the regional RMSE of SST (T02) in the Southern Ocean decreases from 1.27 (1.93) in CTRL experiment to 1.04 (1.67) ℃ in ALL experiment. In boreal summer, the effect is weaker because of the relatively smaller ocean areas in the mid-high latitudes of the Northern Hemisphere.

2. In general, all wave-related processes reduce biases for WSP10s and SWHs, particularly in regions where WSP10s and SWHs were overestimated. The decreased SSTs in VR12-AL-SC-EN stabilize the marine atmospheric boundary layer, and lead to weakened WSP10s and SWHs. The modified roughness in Z0-M04 generally enhances momentum transfer into the ocean, and so decreases WSP10s and SWHs. The relative wind-wave-current speed in FLUX also affects wind stress, and further influences WSP10s and SWHs. Compared with NDBC buoy observations and ERA5, the ALL experiment shows significant improvements.

In addition to the variables aforementioned, the changes of simulated enthalpy fluxes are also compared, which mainly depend on the WSP10s changes. However, the wave-related effects on enthalpy fluxes are non-significant for the 2-month simulation, so the results are not shown.

The wave-related parameterizations used in the study mainly improve model biases at mid-high latitudes, and SST biases in tropical oceans are only slightly improved (Fig. 3&4). Breivik et al. (2015) improved SST as well as subsurface temperature simulations in Nucleus for European Modelling of the Ocean (NEMO) with parametrizations including the wave-related Charnock parameter, modification of water-side stress with wind input and wave dissipation, wave dissipation-related turbulent kinetic energy flux and the Stokes-Coriolis force. Based on a global NEMO-WW3 coupled framework, Couvelard et al. (2020) modified the Charnock parameter, the Stokes drift-related forces and the Langmuir cell with misalignment of winds and waves, the oceanic surface momentum flux and the turbulence kinetic energy to reduce SST and MLD biases. In addition, sea sprays can enhance air-sea heat fluxes in the tropics (Andreas et al. 2008; Andreas et al. 2015). We will consider more processes in future studies.

Different parameterizations for the same wave-related process also deserve discussion. For ocean surface roughness, the most classic parametrizations are those developed by Janssen (1989, 1991), Taylor

and Yelland (2001) and Drennan et al. (2003). The method of Taylor and Yelland (2001) requires the peak wavelength for the total spectrum, whereas that of Drennan et al. (2003) only requires the peak of wind-sea waves. This difference leads to the fact that the former is more suitable for a mixed sea state, while the latter is more suitable for a young sea state (Drennan et al., 2005). And the effect of Janssen's parameterization (1989, 1991) is similar to that of Drennan et al. (2003), since it is also based on the wind-sea conditions (Shimura et al., 2017).

Our case studies indicate that there remain significant biases in the coupled system, probably owing to inaccuracy of coarse resolution, absence of a coupled wave-ice modular, and deficiency of initial fields. In addition, every individual model component could be further improved via new parameter settings or updated parametrization schemes. All these aspects will need to be considered for improving our coupled system.

Code and data availability

The code developed for the coupled system can be found under https://doi.org/10.5281/zenodo.5811002 (Shi et al., 2021), including the coupling, preprocessing, run control and postprocessing scripts. The initial fields for CFSv2.0 are generated by the real time operational Climate Data Assimilation System, downloaded from the CFSv2.0 official website (http://nomads.ncep.noaa.gov/pub/data/nccf/com/cfs/prod). The daily average satellite Optimum Interpolation SST (OISST) data are obtained from NOAA (https://www.ncdc.noaa.gov/oisst), and the National Data Buoy Center (NDBC) buoy data are also obtained from NOAA (https://www.ndbc.noaa.gov). The Argo observational profiles of T/S are available at China Argo Real-time Data Center (www.argo.org.cn). The ERA5 reanalysis are available at the Copernicus Climate

Change Service (C3S) Climate Date Store (https://cds.climate.copernicus.eu/cdsapp#!/dataset/reanalysis-era5-single-levels).

Author contribution

FX and RS designed the experiments and RS carried them out. RS developed the code of coupling parametrizations and produced the figures. ZF contributed to the installation and operation of CFSv2.0. LL and HY contributed to the application of C-Coupler2. XL and YZ provided the original code of CFSv2.0. RS prepared the manuscript with contributions from all co-authors. FX and HL contributed to review and editing.

Acknowledgments

The authors would like to extend thanks to all developers of the CFSv2.0 model (https://cfs.ncep.noaa.gov/cfsv2/downloads.html). The work was supported by National Key Research and Development Program of China (no. 2016YFC1401408), and Tsinghua University Initiative Scientific Research Program (2019Z07L01001). We thank Professor Wei Xue and Professor Yao Liu for helping us test the coupling frequency. We also thank three anonymous reviewers and the handling editor for their constructive comments.

References

Andreas, E. L., Mahrt, L., and Vickers, D.: An improved bulk air-sea surface flux algorithm, including spray-mediated transfer, Quarterly Journal of the Royal Meteorological Society, 141, 642-654, 2015.

Andreas, E. L., Persson, P. O. G., and Hare, J. E.: A bulk turbulent air-sea flux algorithm for high-wind, spray conditions, Journal of Physical Oceanography, 38, 1581-1596, 2008.

Ardhuin, F., Rogers, E., Babanin, A. V., Filipot, J., Magne, R., Roland, A., Der Westhuysen, A. V., Queffeulou, P., Lefevre, J. M., and Aouf, L.: Semiempirical Dissipation Source Functions for Ocean Waves. Part I: Definition, Calibration, and Validation, Journal of Physical Oceanography, 40, 1917-1941, http://dx.doi.org/10.1175/2010JPO4324.1, 2010.

Atlas, R., Hoffman, R. N., Ardizzone, J., Leidner, S. M., Jusem, J. C., Smith, D. K., and Gombos, D.: A Cross-calibrated, Multiplatform Ocean Surface Wind Velocity Product for Meteorological and Oceanographic Applications, Bulletin of the American Meteorological Society, 92, 157-174, http://dx.doi.org/10.1175/2010BAMS2946.1, 2011.

Bao, Y., Song, Z., & Qiao, F.: FIO-ESM version 2.0: Model description and evaluation. Journal of Geophysical Research: Oceans, 125, e2019JC016036. https://doi.org/10.1029/2019JC016036, 2019.

Belcher, S. E., Grant, A. L. M., Hanley, K., Foxkemper, B., Van Roekel, L., Sullivan, P. P., Large, W. G., Brown, A. R., Hines, A., and Calvert, D.: A global perspective on Langmuir turbulence in the ocean surface boundary layer, Geophysical Research Letters, 39, http://dx.doi.org/10.1029/2012GL052932, 2012.

Beljaars, A. C. M.: The parametrization of surface fluxes in large-scale models under free convection. Q. J. R. Meteorol. Soc., 121, 255{270. https://doi.org/10.1002/qj.49712152203, 1994.

Belmonte Rivas, M., and Stoffelen, A.: Characterizing ERA-Interim and ERA5 surface wind biases using ASCAT, Ocean Science, 15, 831-852, 10.5194/os-15-831-2019, 2019.

Bidlot, J.-R., Prates, F., Ribas, R., et al.: Enhancing tropical cyclone wind forecasts, ECMWF newsletter, 164, 33-37. https://www.ecmwf.int/en/newsletter/164/meteorology/enhancing-tropical-cyclonewind-forecasts, 2020.

Bidlot, J.-R.: Model upgrade improves ocean wave forecasts. ECMWF newsletter, 159, 10-10. https://www.ecmwf.int/en/newsletter/159/news/modelupgrade-improves-ocean-wave-forecasts, 2019.

Bidlot, J.-R.: Present status of wave forecasting at ECMWF, Workshop on ocean waves, 25-27, 2012.

Breivik, Ø., Bidlot, J.-R., and Janssen, P. A.: A Stokes drift approximation based on the Phillips spectrum, Ocean Modelling, 100, 49-56, 2016.

Breivik, Ø., Janssen, P. A., and Bidlot, J.-R.: Approximate Stokes drift profiles in deep water, Journal of Physical Oceanography, 44, 2433-2445, 2014.

Breivik, Ø., Mogensen, K., Bidlot, J., Balmaseda, M., and Janssen, P. A. E. M.: Surface wave effects in the NEMO ocean model: Forced and coupled experiments, Journal of Geophysical Research, 120, 2973-2992, http://dx.doi.org/10.1002/2014JC010565, 2015.

Charnock, H.: Wind stress on a water surface, Quarterly Journal of the Royal Meteorological Society, 81, 639-640, http://dx.doi.org/10.1002/qj.49708135027, 1955.

Couvelard, X., Lemarié, F., Samson, G., Redelsperger, J.-L., Ardhuin, F., Benshila, R., and Madec, G.: Development of a two-way-coupled ocean-wave model: assessment on a global NEMO(v3.6)-WW3(v6.02) coupled configuration, Geosci. Model Dev., 13, 3067-3090, https://doi.org/10.5194/gmd-13-3067-2020, 2020.

de Boyer Montégut, C., Madec, G., Fischer, A. S., Lazar, A., and Iudicone, D.: Mixed layer depth over the global ocean: An examination of profile data and a profile - based climatology, Journal of Geophysical Research, 109, http://dx.doi.org/10.1029/2004JC002378, 2004.

Donelan, M. A., Haus, B. K., Reul, N., Plant, W. J., Stiassnie, M., Graber, H. C., Brown, O. B., and Saltzman, E. S.: On the limiting aerodynamic roughness of the ocean in very strong winds, Geophysical Research Letters, 31, 10.1029/2004gl019460, 2004.

543 Drennan, W. M., H. C. Graber, D. Hauser, and C. Quentin: On the wave age dependence of wind stress
544 over pure wind seas, J. Geophys. Res., 108(C3), 8062, doi:10.1029/2000JC000715, 2003.
545 Drennan, W. M., P. K. Taylor, and M. J. Yelland: Parameterizing the sea surface roughness, J. Phys.
546 Oceanogr., 35(5), 835-848, 2005.
547 ECMWF: Official IFS Documentation CY47R1. In chap. PART VII: ECMWF wave model. Reading,
548 UK: ECMWF, 10.21957/31drbygag, 2020.
549 Fan, Y., Lin, S., Held, I. M., Yu, Z., and Tolman, H. L.: Global Ocean Surface Wave Simulation Using a
550 Coupled Atmosphere-Wave Model, Journal of Climate, 25, 6233-6252, http://dx.doi.org/10.1175/JCLI-
551 D-11-00621.1, 2012.
552 Ghantous, M., and Babanin, A. V.: One-dimensional modelling of upper ocean mixing by turbulence due
553 to wave orbital motion, Nonlinear Processes in Geophysics, 21, 325-338, 10.5194/npg-21-325-2014,
554 2014.
555 Griffies, S. M., Harrison, M. J., Pacanowski, R. C., and Rosati, A.: A technical guide to MOM4, GFDL
556 Ocean Group Tech. Rep, 5, 342, 2004.
557 Hasselmann, K.: Wave-driven inertial oscillations, Geophysical and Astrophysical Fluid Dynamics, 1,
558 463-502, http://dx.doi.org/10.1080/03091927009365783, 1970.
559 Hersbach H. and Bidlot, J.-R.: The relevance of ocean surface current in the ECMWF analysis and
560 forecast system. Proceeding from the ECMWF Workshop on Atmosphere-Ocean Interaction, 10-12,
561 https://www.ecmwf.int/sites/default/files/elibrary/2009/9866-relevance-ocean-surface-current-ecmwf-
562 analysis-and-forecast-system.pdf, 2008.
563 Hersbach, H., Bell, B., Berrisford, P., Hirahara, S., et al.: The ERA5 Global Reanalysis, Quarterly Journal
564 of the Royal Meteorological Society, Soc. 00: 363 (2020), https://doi.org/10.1002/qj.3803, 2020.

565 Hsu, S. A., Eric A. Meindl, and David B. Gilhousen: Determining the Power-Law Wind-Profile Exponent
566 under Near-Neutral Stability Conditions at Sea, Applied Meteorology, Vol. 33, No. 6,
567 https://doi.org/10.1175/1520-0450(1994)033<0757:DTPLWP>2.0.CO;2, 1994.
568 Janssen, P. A. E. M.: The interaction of ocean waves and wind, Cambridge University Press, pp 312,
569 2004.
570 Janssen, P. A. E. M.: The Quasi-linear theory of wind wave generation applied to wave forecasting. J.
571 Phys. Oceanogr. 21, 1631-1642. https://doi.org/10.1175/1520-
572 0485(1991)021<1631:QLTOWW>2.0.CO;2, 1991.
573 Janssen, P. A. E. M.: Wave-induced stress and the drag of air flow over sea waves. J. Phys. Oceanogr.
574 19(6), 745-754. https://doi.org/10.1175/1520-1310 0485(1989)019<0745:WISATD>2.0.CO;2, 1989.
575 Kalnay, E., Kanamitsu, M., Kistler, R., Collins, W. D., Deaven, D. G., Gandin, L. S., Iredell, M. D., Saha,
576 S., White, G. H., and Woollen, J.: The NCEP/NCAR 40-Year Reanalysis Project, Bulletin of the
577 American Meteorological Society, 77, 437-471, http://dx.doi.org/10.1175/1520-
578 0477(1996)077%3C0437:TNYRP%3E2.0.CO;2, 1996.
579 Kalverla, P. C., Holtslag, A. A. M., Ronda, R. J., and Steeneveld, G.-J.: Quality of wind characteristics
580 in recent wind atlases over the North Sea, Quarterly Journal of the Royal Meteorological Society, 146,
581 1498-1515, 10.1002/qj.3748, 2020.
582 Kukulka, T., Plueddemann, A. J., Trowbridge, J. H., and Sullivan, P. P.: Significance of Langmuir
583 circulation in upper ocean mixing: comparison of observations and simulations, Geophysical Research
584 Letters, 36, http://dx.doi.org/10.1029/2009GL037620, 2009.
585 Law-Chune, S., and Aouf, L.: Wave effects in global ocean modeling: parametrizations vs. forcing from
586 a wave model, Ocean Dynamics, 68, 1739-1758, http://dx.doi.org/10.1007/s10236-018-1220-2, 2018.

587 Lemarié, F.: Numerical modification of atmospheric models to include the feedback of oceanic currents
588 on air-sea fluxes in ocean-atmosphere coupled models, INRIA Grenoble-Rhône-Alpes, Laboratoire Jean
589 Kuntzmann, https://hal.inria.fr/hal-01184711/document, 2015.
590 Li, D., Staneva, J., Bidlot, J.-R., Grayek, S., Zhu, Y., and Yin, B.: Improving Regional Model Skills
591 During Typhoon Events: A Case Study for Super Typhoon Lingling Over the Northwest Pacific Ocean,
592 Frontiers in Marine Science, 8, 10.3389/fmars.2021.613913, 2021.
593 Li, M., and Garrett, C.: Mixed Layer Deepening Due to Langmuir Circulation, Journal of Physical
594 Oceanography, 27, 121-132, http://dx.doi.org/10.1175/1520-
595 0485(1997)027%3C0121:MLDDTL%3E2.0.CO;2, 1997.
596 Li, Q., Foxkemper, B., Breivik, O., and Webb, A.: Statistical models of global Langmuir mixing, Ocean
597 Modelling, 113, 95-114, http://dx.doi.org/10.1016/j.ocemod.2017.03.016, 2017.
598 Li, Q., Webb, A., Foxkemper, B., Craig, A., Danabasoglu, G., Large, W. G., and Vertenstein, M.:
599 Langmuir mixing effects on global climate: WAVEWATCH III in CESM, Ocean Modelling, 103, 145-
600 160, http://dx.doi.org/10.1016/j.ocemod.2015.07.020, 2016.
601 Li, Z., Liu, Z., & Xing, X.: User Manual for Global Argo Observational data set (V3.0) (1997-2019),
602 China Argo Real-time Data Center, Hangzhou, 37pp, 2019.
603 Liu, L., Zhang, C., Li, R., and Wang, B.: C-Coupler2: a flexible and user-friendly community coupler for
604 model coupling and nesting, Geoscientific Model Development Discussions, 11, 1-63,
605 http://dx.doi.org/10.5194/gmd-11-3557-2018, 2018.
606 Luo, J.J., Masson, S., Roeckner, E., Madec, G., & Yamagata, T.: Reducing climatology Bias in an ocean-
607 atmosphere CGCM with improved coupling physics. Journal of Climate, 18(13), 2344-2360.
608 https://doi.org/10.1175/JCLI3404.1, 2005.

609 Mcwilliams, J. C., and Sullivan, P. P.: Vertical Mixing by Langmuir Circulations, Spill Science &
610 Technology Bulletin, 6, 225-237, http://dx.doi.org/10.1016/S1353-2561(01)00041-X, 2000.
611 Monin, A. S., and Obukhov, A. M.: Basic laws of turbulent mixing in the surface layer of the atmosphere,
612 Contrib. Geophys. Inst. Acad. Sci. USSR, 151(163), e187, 1954.
613 Moon, I., Ginis, I., and Hara, T.: Effect of surface waves on Charnock coefficient under tropical cyclones,
614 Geophysical Research Letters, 31, http://dx.doi.org/10.1029/2004GL020988, 2004.
615 Moum J.N., and Smyth W.D.: Upper Ocean Mixing. In Cochran, J. Kirk; Bokuniewicz, J. Henry; Yager,
616 L. Patricia (Eds.) Encyclopedia of Ocean Sciences, 3rd Edition. vol. 1, pp. 71-79, Elsevier. ISBN: 978-
617 0-12-813081-0, 2019.
618 O'Neill, L. W., Chelton, D. B., and Esbensen, S. K.: Observations of SST-induced perturbations of the
619 wind stress field over the Southern Ocean on seasonal timescales, Journal of Climate, 16, 2340-2354,
620 10.1175/2780.1, 2003.
621 Pineau-Guillou L., Ardhuin,F., Bouin,M.N.,Redelsperger,J.L.,Chapron,B., Bidlot, J. R., & Quilfen, Y.:
622 Strong winds in a coupled wave-atmosphere model during a North Atlantic storm event: evaluation
623 against observations. Quarterly Journal of the Royal Meteorological Society, 144(711), 317-332, 2018.
624 Polonichko, V.: Generation of Langmuir circulation for nonaligned wind stress and the Stokes drift, J.
625 Geophys. Res., 102, 15773-15780, https://doi.org/10.1029/97JC00460, 1997.
626 Powell, M. D., Vickery, P. J., and Reinhold, T. A.: Reduced drag coefficient for high wind speeds in
627 tropical cyclones, Nature, 422, 279-283, 10.1038/nature01481, 2003.
628 Qiao, F., Yuan, Y., Yang, Y., Zheng, Q., Xia, C., and Ma, J.: Wave‐induced mixing in the upper ocean:
629 Distribution and application to a global ocean circulation model, Geophysical Research Letters, 31,
630 http://dx.doi.org/10.1029/2004GL019824, 2004.

631 Renault, L., Arsouze, T., and Ballabrera-Poy, J.: On the Influence of the Current Feedback to the
632 Atmosphere on the Western Mediterranean Sea Dynamics, Journal of Geophysical Research-Oceans, 126,
633 10.1029/2020jc016664, 2021.
634 Renault, L., Molemaker, M. J., McWilliams, J. C., Shchepetkin, A. F., Lemarie, F., Chelton, D., Illig, S.,
635 and Hall, A.: Modulation of Wind Work by Oceanic Current Interaction with the Atmosphere, Journal of
636 Physical Oceanography, 46, 1685-1704, 10.1175/jpo-d-15-0232.1, 2016.
637 Reynolds, R. W., Smith, T. M., Liu, C., Chelton, D. B., Casey, K. S., and Schlax, M. G.: Daily High-
638 Resolution-Blended Analyses for Sea Surface Temperature, Journal of Climate, 20, 5473-5496,
639 http://dx.doi.org/10.1175/2007JCLI1824.1, 2007.
640 Saha, S., Moorthi, S., Pan, H., Wu, X., Wang, J., Nadiga, S., Tripp, P., Kistler, R., Woollen, J., and
641 Behringer, D.: The NCEP Climate Forecast System Reanalysis, Bulletin of the American Meteorological
642 Society, 91, 1015-1057, http://dx.doi.org/10.1175/2010BAMS3001.1, 2010.
643 Saha, S., Moorthi, S., Wu, X., Wang, J., Nadiga, S., Tripp, P., Behringer, D., Hou, Y., Chuang, H., and
644 Iredell, M. D.: The NCEP Climate Forecast System Version 2, Journal of Climate, 27, 2185-2208,
645 http://dx.doi.org/10.1175/JCLI-D-12-00823.1, 2014.
646 Sauvage, C., Lebeaupin Brossier, C., Bouin, M. N., & Ducrocq, V.: Characterization of the air-sea
647 exchange mechanisms during a Mediterranean heavy precipitation event using realistic sea state
648 modelling. Atmospheric Chemistry & Physics, 20(3), 2020.
649 Sharmar, V., and Markina, M.: Validation of global wind wave hindcasts using ERA5, MERRA2, ERA-
650 Interim and CFSRv2 reanalyzes, IOP Conference Series: Earth and Environmental Science, 606, 012056
651 (012059 pp.)-012056 (012059 pp.), 10.1088/1755-1315/606/1/012056, 2020.

652 Shimura, T., Mori, N., Takemi, T., et al.: Long term impacts of ocean wave-dependent roughness on
653 global climate systems. Journal of Geophysical Research: Oceans, 122(3),
654 https://doi.org/10.1002/2016JC012621, 2017.
655 Stopa, J. E., Ardhuin, F., Babanin, A. V., and Zieger, S.: Comparison and validation of physical wave
656 parameterizations in spectral wave models, Ocean Modelling, 103, 2-17,
657 http://dx.doi.org/10.1016/j.ocemod.2015.09.003, 2016.
658 Sweet, W., Fett, R., Kerling, J., and Laviolette, P.: Air-sea interaction effects in the lower troposphere
659 across the north wall of the Gulf Stream, Mon. Weather Rev., 109, 1042-1052, 10.1175/1520-
660 0493(1981)109<1042:Asieit>2.0.Co;2, 1981.
661 Takatama, K., and Schneider, N.: The Role of Back Pressure in the Atmospheric Response to Surface
662 Stress Induced by the Kuroshio, Journal of the Atmospheric Sciences, 74, 597-615, 10.1175/jas-d-16-
663 0149.1, 2017.
664 Taylor, P. K., and Yelland, M. J.: The Dependence of Sea Surface Roughness on the Height and Steepness
665 of the Waves, Journal of Physical Oceanography, 31, 572-590, http://dx.doi.org/10.1175/1520-
666 0485(2001)031%3C0572:TDOSSR%3E2.0.CO;2, 2001.
667 Terray, E. A., Donelan, M. A., Agrawal, Y. C., Drennan, W. M., Kahma, K. K., Williams, A. J., Hwang,
668 P. A., and Kitaigorodskii, S. A.: Estimates of Kinetic Energy Dissipation under Breaking Waves, Journal
669 of Physical Oceanography, 26, 792-807, http://dx.doi.org/10.1175/1520-
670 0485(1996)026%3C0792:EOKEDU%3E2.0.CO;2, 1996.
671 Tolman, H. L., and Chalikov, D. V.: Source Terms in a Third-Generation Wind Wave Model, Journal of
672 Physical Oceanography, 26, 2497-2518, http://dx.doi.org/10.1175/1520-
673 0485(1996)026%3C2497:STIATG%3E2.0.CO;2, 1996.

Van Roekel, L. P., Foxkemper, B., Sullivan, P. P., Hamlington, P. E., and Haney, S.: The form and orientation of Langmuir cells for misaligned winds and waves, Journal of Geophysical Research, 117, http://dx.doi.org/10.1029/2011JC007516, 2012.

Wang, L., and Xu, F.: Decadal variability and trends of oceanic barrier layers in tropical Pacific, Ocean Dynamics, 68, 1155-1168, 10.1007/s10236-018-1191-3, 2018.

WAVEWATCH III Development Group.: User manual and system documentation of WAVEWATCH III version 5.16, NOAA/NWS/NCEP/MMAB Technical Note 329, 326, 2016.

Wu, L., Staneva, J., Breivik, Ø., Rutgersson, A., Nurser, A. G., Clementi, E., and Madec, G.: Wave effects on coastal upwelling and water level, Ocean Modelling, 140, 101405, 2019.

Wu, X., K. S. Moorthi, K. Okomoto, and H. L. Pan: Sea ice impacts on GFS forecasts at high latitudes, Proceedings of the 85th AMS Annual Meeting, 8th Conference on Polar Meteorology and Oceanography, San Diego, CA, 2005.

Zieger, S., Babanin, A. V., Rogers, W. E., and Young, I. R.: Observation-based source terms in the third-generation wave model WAVEWATCH, Ocean Modelling, 96, 2-25, http://dx.doi.org/10.1016/j.ocemod.2015.07.014, 2015.

Table 1. List of numerical experiments: setups different from CTRL are marked with bold

Experiments	Physical Process/Parameterization		
	Langmuir Cell with Stokes-Coriolis Force and Entrainment	Roughness (Charnock Parameter)	Relative Velocity in Flux
CTRL	Off	Off	Off
VR12-AL-SC-EN	**Eqn. 1-6, 8-10**	Off	Off
Z0-M04	Off	**C_{ch} from Eqn. 16, 17**	Off
FLUX	Off	Off	**$\Delta\vec{V}$ from Eqn. 14**
ALL	**Eqn. 1-6, 8-10**	**C_{ch} from Eqn. 16, 17**	**$\Delta\vec{V}$ from Eqn. 14**

Table 2. The 53-day mean bias with standard deviation (STD) and RMSE for WSP10 and SWH compared with NDBC buoy observation: the bias is calculated as simulation minus NDBC.

Boreal Winter WSP10	**Bias with STD**	**RMSE**
CTRL	0.16±1.23	1.24
VR12-AL-SC-EN	0.01±1.12	1.12
Z0-M04	-0.01±1.07	1.07
FLUX	0.39±1.20	1.26
ALL	0.07±1.04	1.04
Boreal Winter SWH	**Bias with STD**	**RMSE**
CTRL	0.21±0.38	0.44
VR12-AL-SC-EN	0.14±0.35	0.37
Z0-M04	0.10±0.30	0.32
FLUX	0.24±0.34	0.42
ALL	0.12±0.34	0.36
Boreal Summer WSP10	**Bias with STD**	**RMSE**
CTRL	0.15±1.23	1.24
VR12-AL-SC-EN	-0.03±1.22	1.22
Z0-M04	-0.04±1.21	1.21
FLUX	-0.22±1.18	1.20
ALL	-0.17±1.14	1.15
Boreal Summer SWH	**Bias with STD**	**RMSE**
CTRL	0.28±0.25	0.38
VR12-AL-SC-EN	0.19±0.24	0.30
Z0-M04	0.22±0.26	0.34
FLUX	0.14±0.25	0.29
ALL	0.12±0.21	0.24

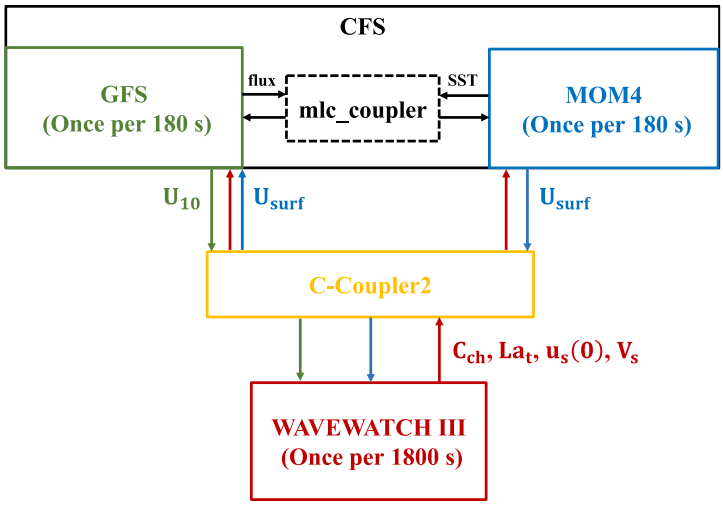

Figure 1. A schematic diagram of the atmosphere-ocean-wave coupled modeling system. The arrows indicate the coupled variables that are passed between the model components. In the diagram, C_{ch}, La_t, $u_s(0)$, V_s, U_{10}, and U_{surf} are Charnock parameter (red arrows), turbulent Langmuir number (red arrows), surface Stokes drift velocity (red arrows), Stokes transport (red arrows), 10-m wind (green arrows) and surface current (blue arrows), respectively.

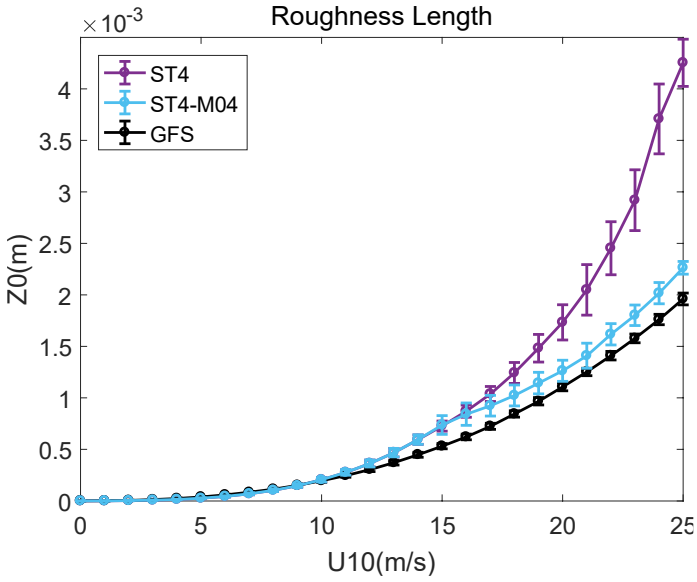

Figure 2. Relationships between momentum roughness length z_0 (m) in the coupled system and 10-m wind speed (m/s); error bars indicate twice the standard deviations for each point.

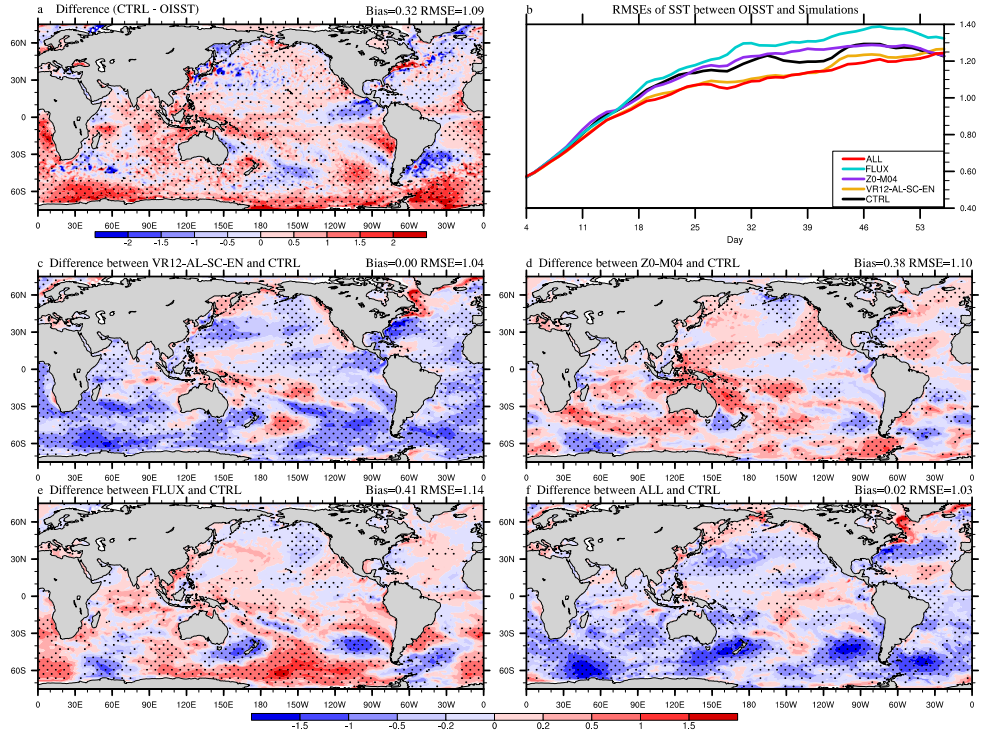

Figure 3. The 53-day average SST (°C) bias in CTRL (a; CTRL minus OISST), the time series of global-averaged RMSE (b), and the differences between VR12-AL-SC-EN (c)/Z0-M04 (d)/ FLUX (e)/ ALL (f) and CTRL in Jan-Feb, 2017 (VR12-AL-SC-EN/Z0-M04/FLUX/ALL minus CTRL). The first 3-day simulation is discarded. The dotted areas are statistically significant at 95% confidence level.

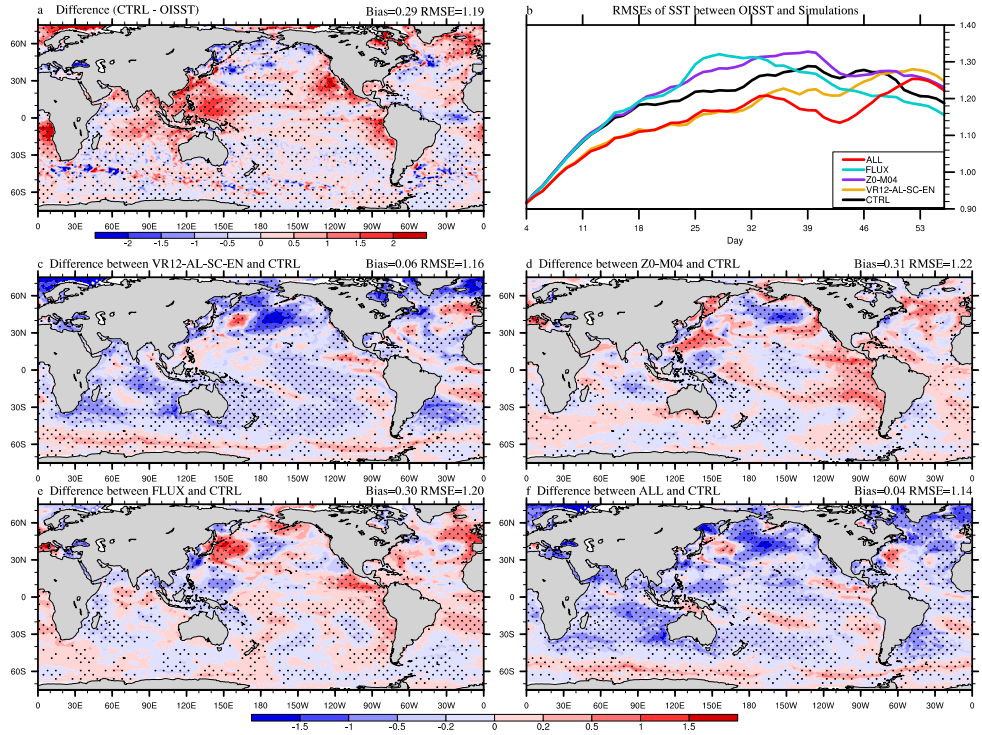

Figure 4. The same as Figure 3 but for Aug-Sep, 2018.

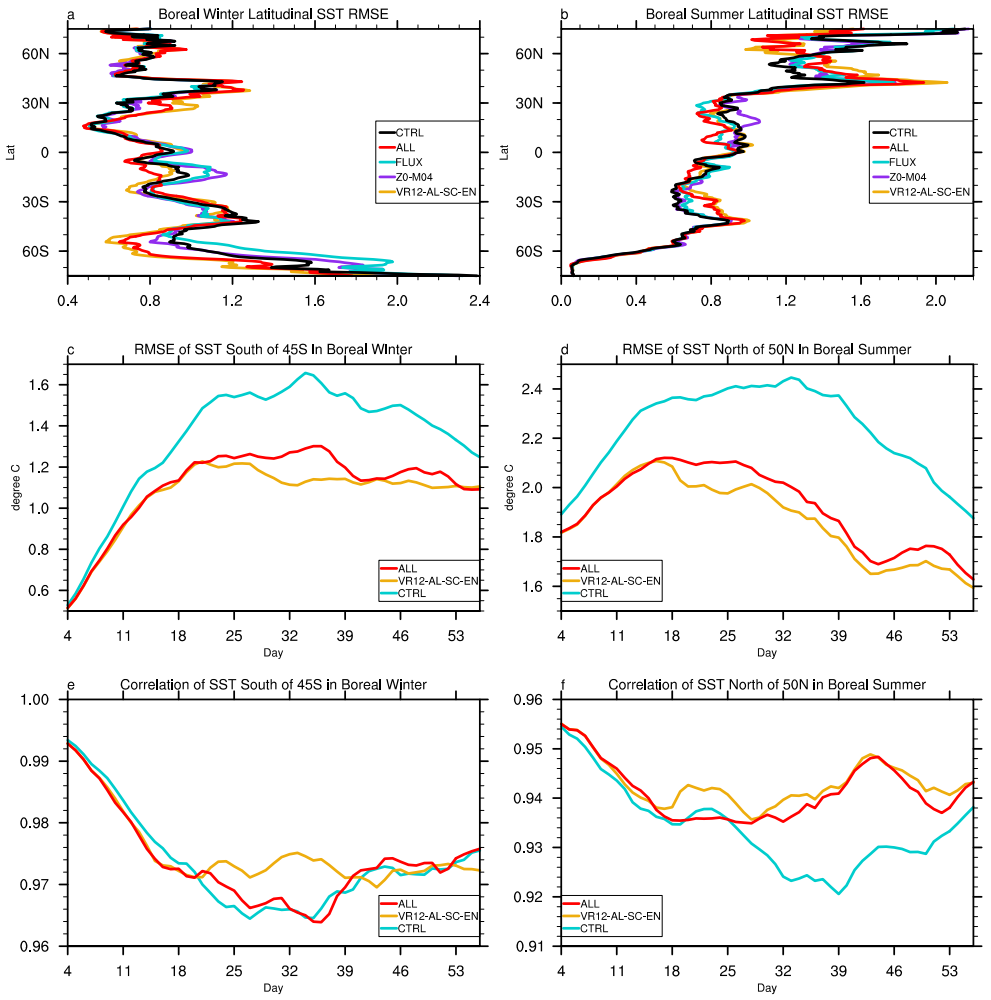

Figure 5. The 53-day averaged latitudinal distribution of SST root mean square errors (RMSE), time series of domain-averaged SST RMSE and correlation coefficient: **a/b** the latitudinal RMSE in boreal winter/summer compared with OISST, **c/d** the time series of domain-averaged (0-360°E, 45-78°S/50-78°N) SST RMSE in boreal winter/summer, **e/f** the time series of domain-averaged (0-360°E, 45-78°S/50-78°N) SST correlation coefficient in boreal winter/summer; differences of RMSE and correlation coefficient time series between VR12-AL-SC-EN/ALL and CTRL are statistically significant at 99% confidence level, except those in Fig. e.

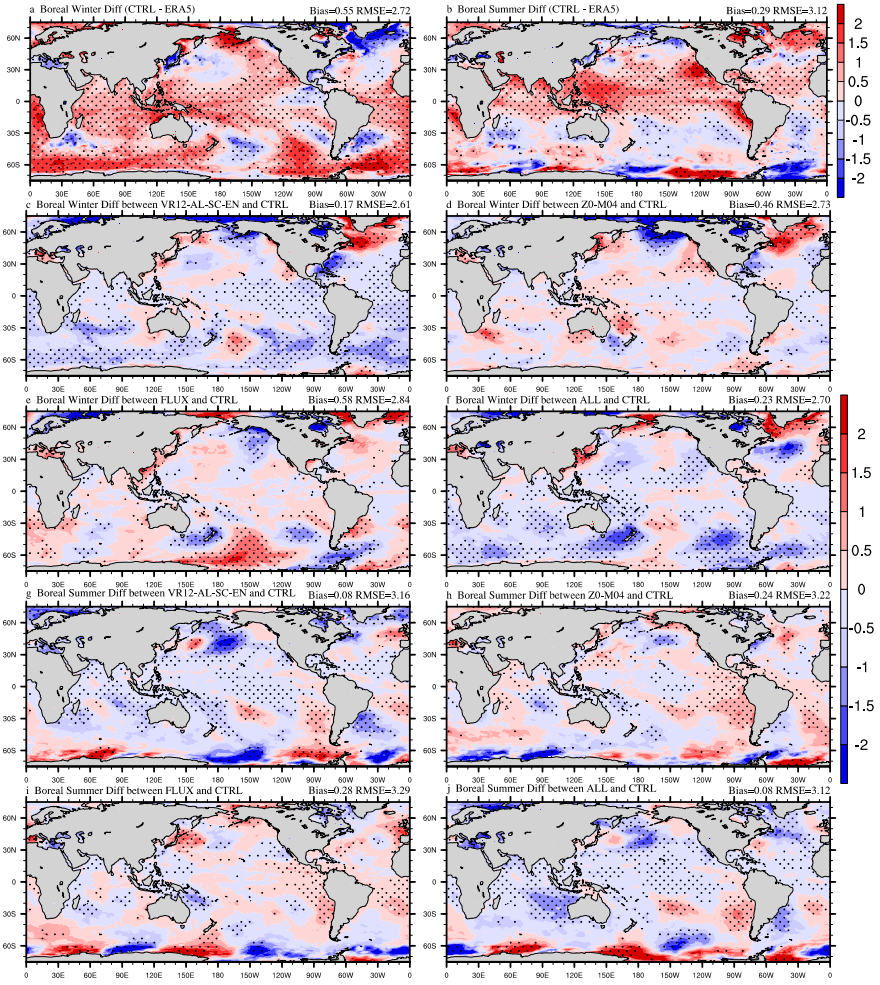

Figure 6. The 53-day average T02 (°C) bias in CTRL (a&b; CTRL minus ERA5), and the differences between VR12-AL-SC-EN (c&g)/Z0-M04 (d&h)/ FLUX (e&i)/ ALL (f&j) and CTRL (VR12-AL-SC-EN/Z0-M04/FLUX/ALL minus CTRL). The first 3-day simulation is discarded. The dotted areas are statistically significant at 95% confidence level. a/c/d/e/f are for Jan-Feb, 2017, and b/g/h/i/j are for Aug-Sep, 2018.

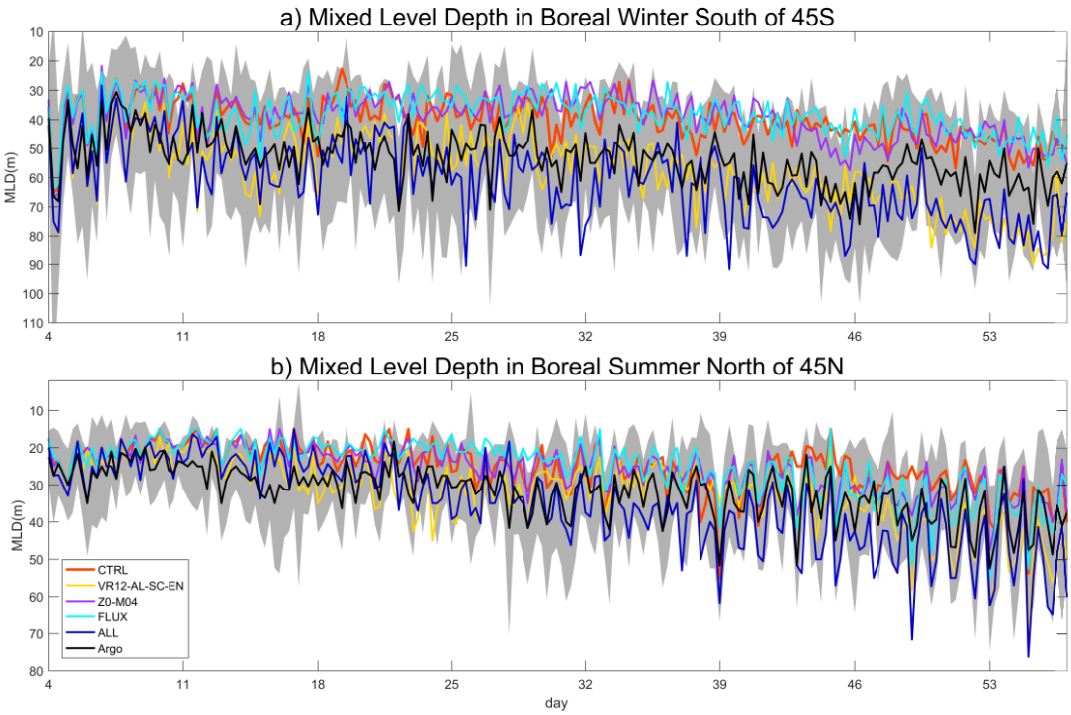

Figure 7. The 53-day time series of domain-averaged (0-360°E, 45-78°S/N) mixed layer depth (MLD; m) in boreal winter/summer: the difference between CTRL and VR12-AL-SC-EN/ALL passes the student's t-test at 99% confidence level; the time intervals are 6 hours; shaded areas indicate twice the standard deviations for Argo.

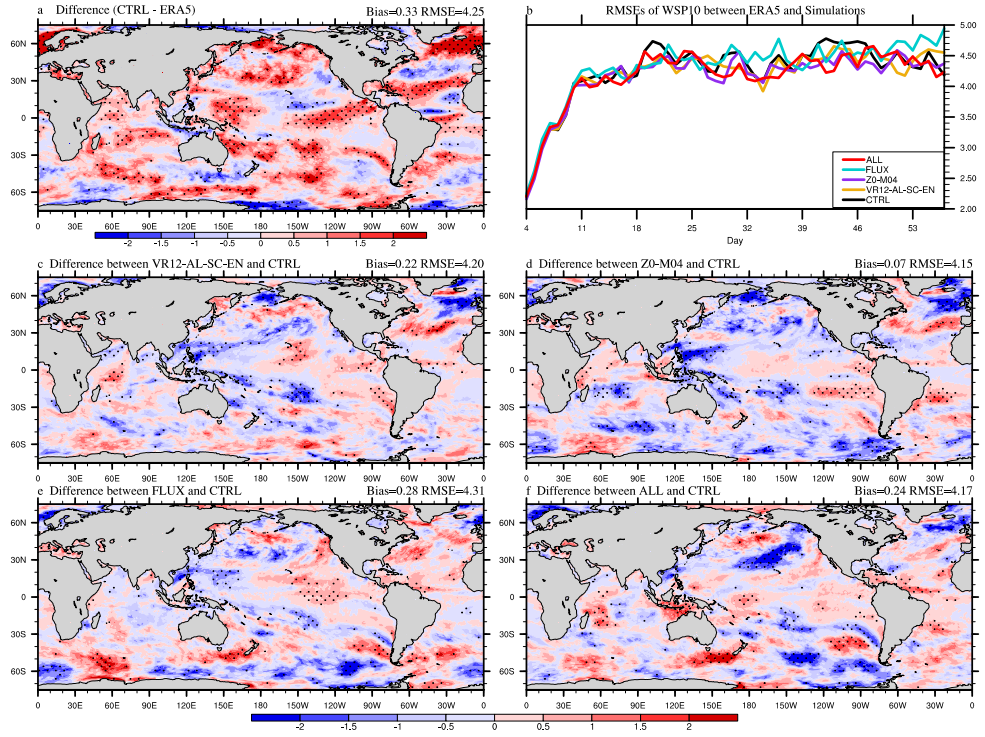

Figure 8. The 53-day average WSP10 (m/s) bias in CTRL (a; CTRL minus ERA5), the time series of global-averaged RMSE (b), and the differences between VR12-AL-SC-EN (c)/Z0-M04 (d)/ FLUX (e)/ ALL (f) and CTRL in Jan-Feb, 2017 (VR12-AL-SC-EN/Z0-M04/FLUX/ALL minus CTRL). The first 3-day simulation is discarded. The dotted areas are statistically significant at 95% confidence level.

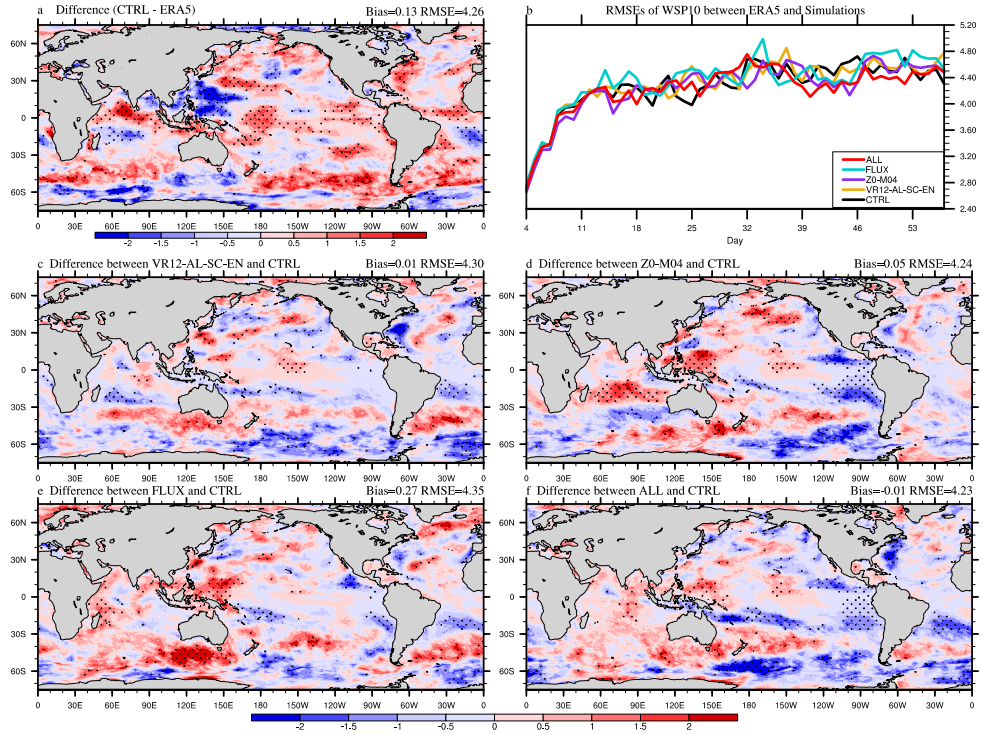

Figure 9. The same as Figure 8 but for Aug-Sep, 2018.

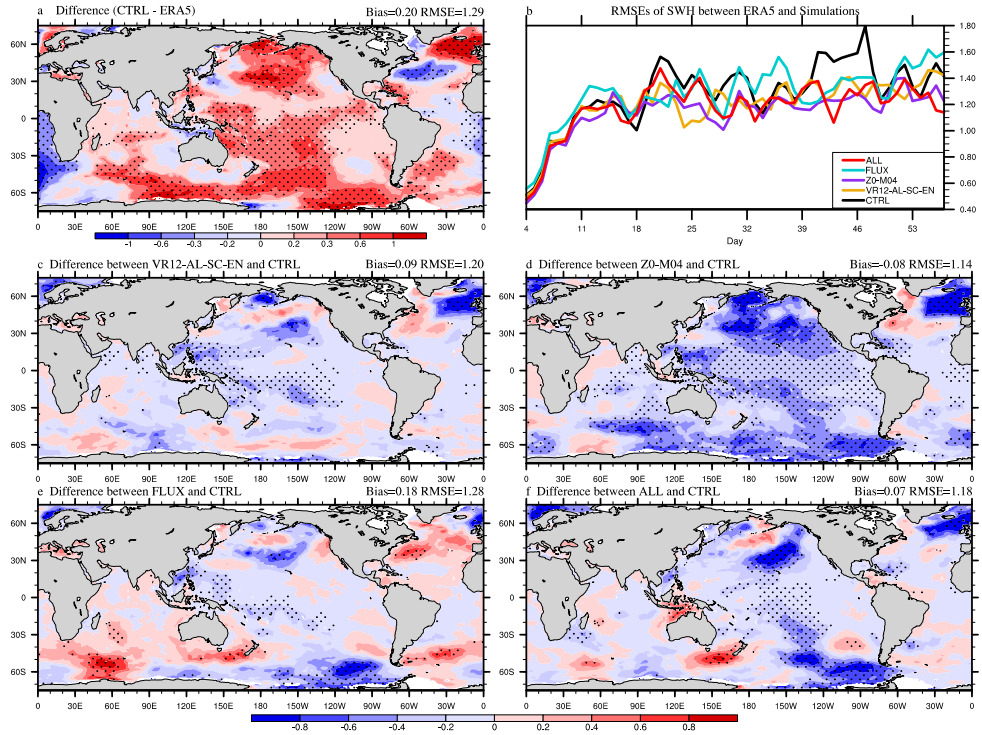

Figure 10. The 53-day average SWH (m) bias in CTRL (a; CTRL minus ERA5), the time series of global-averaged RMSE (b), and the differences between VR12-AL-SC-EN (c)/Z0-M04 (d)/ FLUX (e)/ ALL (f) and CTRL in Jan-Feb, 2017 (VR12-AL-SC-EN/Z0-M04/FLUX/ALL minus CTRL). The first 3-day simulation is discarded. The dotted areas are statistically significant at 95% confidence level.

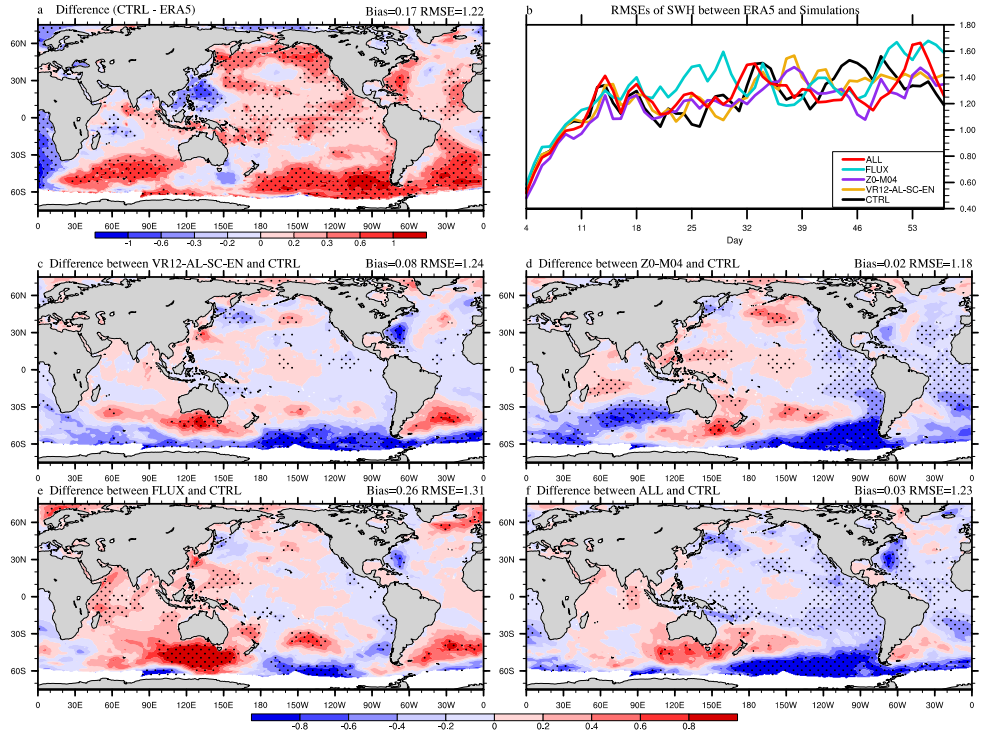

Figure 11. The same as Figure 10 but for Aug-Sep, 2018.

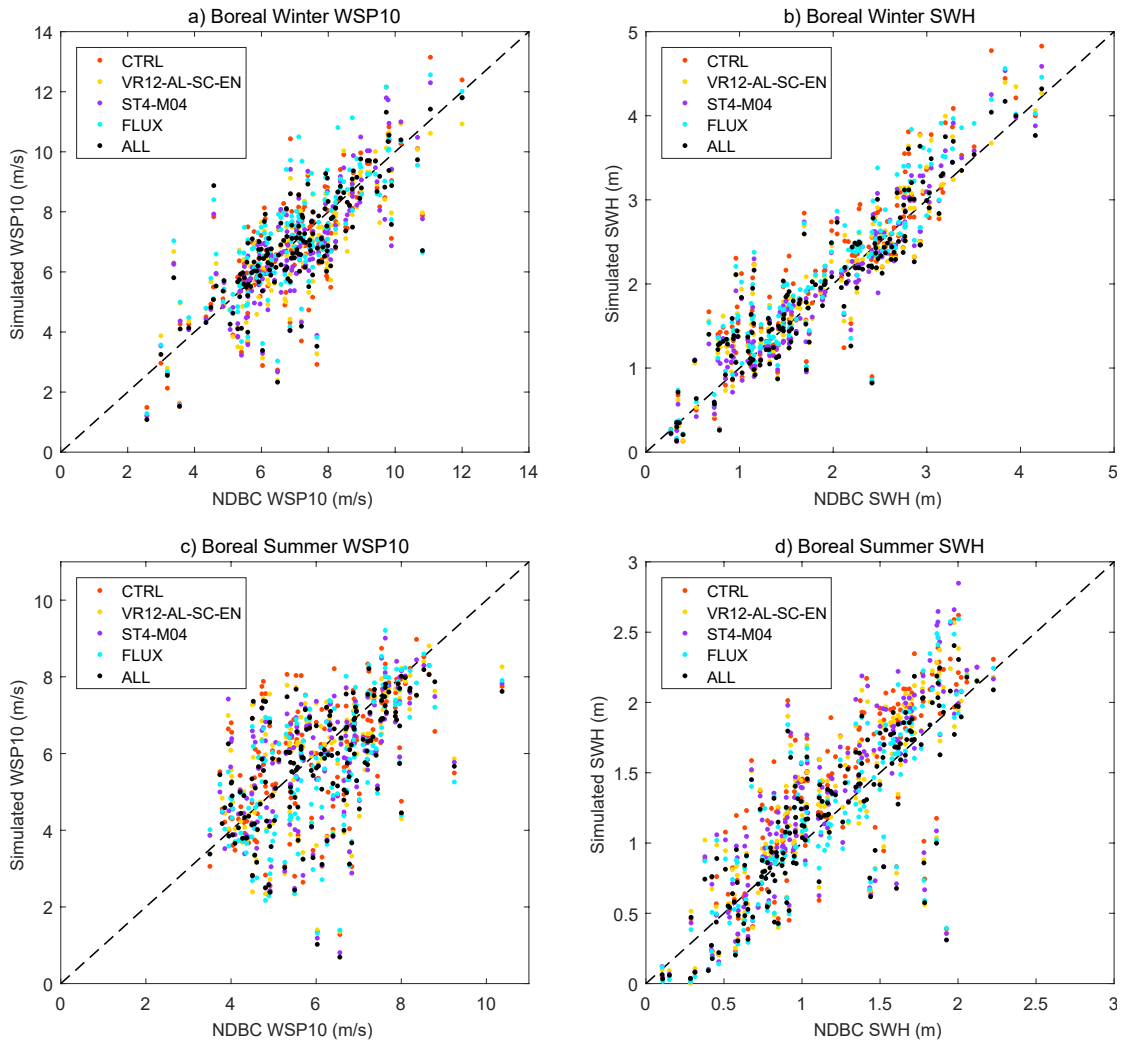

Figure 12. Scatter plots of simulated WSP10/SWH (y-axis) vs buoy WSP10/SWH (x-axis): (a) the WSP10 in Jan-Feb, 2017, (b) the SWH in Jan-Feb, 2017, (c) the WSP10 in Aug-Sep, 2018, and (d) the SWH in Aug-Sep, 2018. The dotted line is y=x. The corresponding mean biases with standard deviations and RMSEs for every experiment are shown in Table 2.